Ultrahigh Thermoelectric Figure of Merit and Enhanced Mechanical Stability of p-type AgSb$_{1-x}$Zn$_x$Te$_2$

Subhajit Roychowdhury, Rajarshi Panigrahi, Suresh Perumal, and Kanishka Biswas*[●]

New Chemistry Unit, Jawaharlal Nehru Centre for Advanced Scientific Research (JNCASR), Jakkur P.O., Bangalore 560 064, India

[S] *Supporting Information*

ABSTRACT: High-performance thermoelectric materials are desirable in the lower-medium temperature range (450−650 K) for low-grade waste heat recovery. We report a thermoelectric figure of merit (zT) of 1.9 at 585 K in p-type AgSb$_{1-x}$Zn$_x$Te$_2$, which is the highest value measured among the p-type materials in the 450−650 K range. A high average thermoelectric figure of merit (zT$_{avg}$) of 1.3 is achieved in AgSb$_{0.96}$Zn$_{0.04}$Te$_2$. Moreover, the AgSb$_{1-x}$Zn$_x$Te$_2$ sample exhibits a hardness value of ∼6.3 GPa (nanoindentation), which is significantly higher than that of the pristine AgSbTe$_2$. Substitution of Zn in AgSbTe$_2$ suppresses the formation of intrinsic Ag$_2$Te impurity phases, which indeed increases the thermal and mechanical stability. The lattice thermal conductivity for AgSb$_{1-x}$Zn$_x$Te$_2$ samples is reasonably reduced compared to that of the pristine AgSbTe$_2$ because of the significant solid solution point defect phonon scattering. Aliovalent Zn^{2+} doping in Sb^{3+} sites in AgSbTe$_2$ increases the p-type carrier concentration, which boosts the electrical conductivity of AgSb$_{1-x}$Zn$_x$Te$_2$.
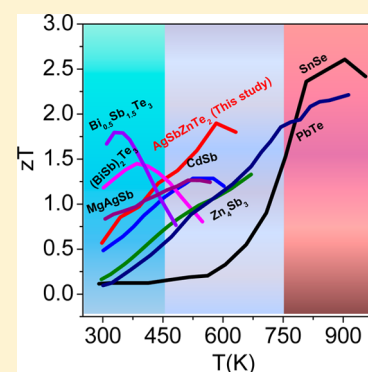
Thermoelectric (TE) materials are a potential candidate for waste heat to electrical energy conversion. The efficiency of thermoelectric materials depends on dimensionless figure of merit, zT = $\sigma S^2 T/\kappa$, where σ, S, κ, and T are electrical conductivity, Seebeck coefficient, total thermal conductivity, and temperature, respectively.[1−5] It is a great challenge to improve overall zT by simultaneous optimization of σ, S, and κ because of their interdependent nature. Higher power factor (σS^2) and/or lower thermal conductivity are necessary for the enhancement of zT. Significant efforts have been made to improve the Seebeck coefficient via introduction of resonance levels in electronic bands near the Fermi level[6,7] and convergence of electronic band valleys.[8−10] On the other hand, recent advances show that high thermoelectric performance could be achieved mainly through the remarkable decrease in the lattice thermal conductivity via phonon scattering by introducing solid solution point defects, second phase nanoprecipitates,[11−13] mesoscale grain boundaries,[14,15] intrinsic bond anharmonicity,[16−20] and rattling modes.[19,20]

AgSbTe$_2$ is considered to be a promising thermoelectric material for power generation application in the temperature range of 400−700 K because of its glasslike anomalously low thermal conductivity (0.6−0.7 W m^{-1} K^{-1}).[17,21−24] At room temperature, AgSbTe$_2$ crystallizes in a disordered rock-salt structure (space group, $Fm\overline{3}m$) in which Ag and Sb randomly occupy the cation site and Te occupies the anion site.[25] Previous studies indicate that strong anharmonicity in Sb−Te

bonds is responsible for ultralow thermal conductivity, which is mainly caused by the existence of the stereochemically active 5s^2 lone pair on Sb.[23] Moreover, narrow band gap semiconductor, AgSbTe$_2$, exhibits p-type conduction with high thermopower due to the presence of multiple flat valence band valleys.[26] Notably, alloys of AgSbTe$_2$ with PbTe-rich [(AgSbTe$_2$)$_{1-x}$(PbTe)$_x$ (LAST)][27] and GeTe rich [(AgSbTe$_2$)$_{1-x}$(GeTe)$_x$ (TAGS)][28] phases are famous for their excellent thermoelectric performance.

Thermoelectric materials must be thermodynamically stable and mechanically robust for long-term applications. Despite its high thermoelectric performances, thermodynamic stability of AgSbTe$_2$ has remained a challenging issue since its discovery.[29,30] Detailed studies on pseudobinary Sb$_2$Te$_3$−Ag$_2$Te and Sb$_2$Te$_3$−Ag$_2$Te−Te phase diagrams confirm the non-existence of a thermodynamically stable compound with the exact stoichiometric composition of AgSbTe$_2$.[31−33] A stable cubic phase with a wide range of compositions (Ag$_{1-x}$Sb$_{1+x}$Te$_{2+x}$; x = 0.06−0.28) is the only ternary compound in the Sb$_2$Te$_3$−Ag$_2$Te phase diagram.[18] This nonstoichiometric AgSbTe$_2$ slowly decomposes into a solid solution of Ag in Sb$_2$Te$_3$ and solid solution of Sb in β-Ag$_2$Te at 630 K.[31−34] Moreover, several groups have reported the presence of a small amount of α-Ag$_2$Te as a second phase in AgSbTe$_2$ at room temperature
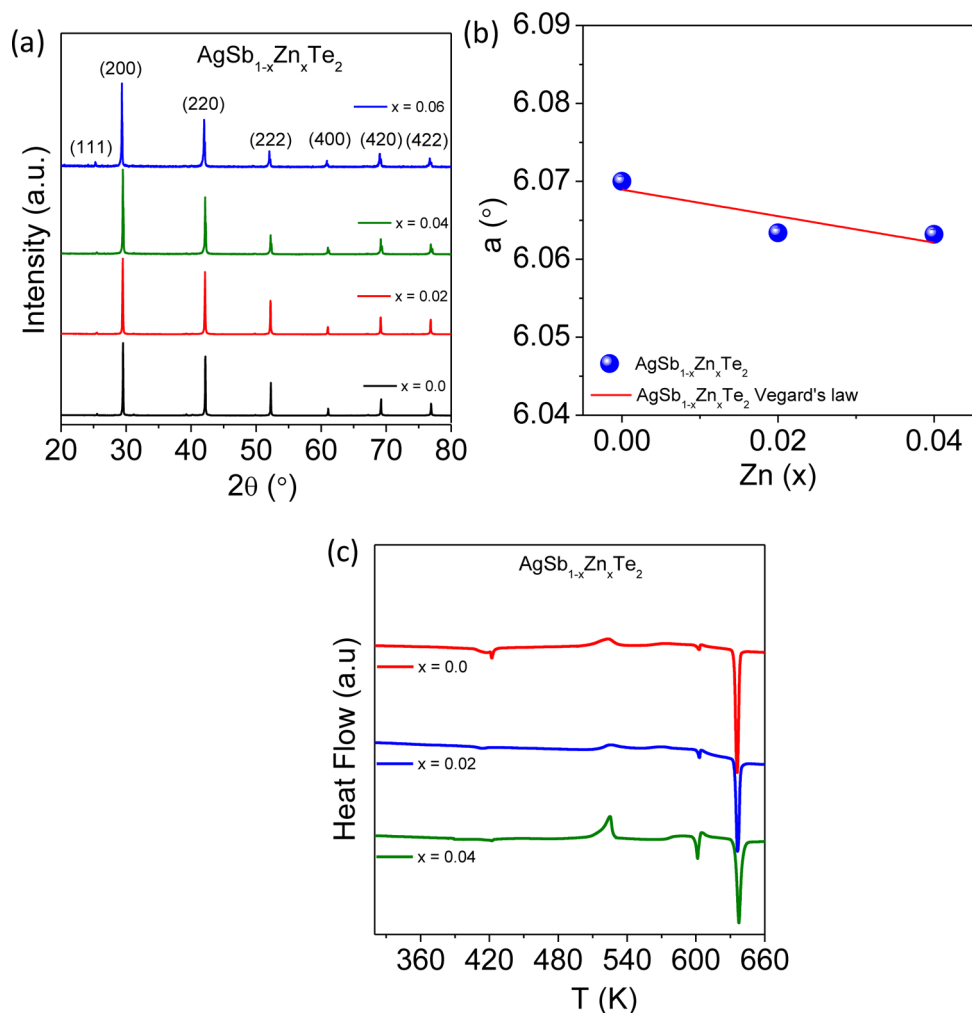
Figure 1. (a) Powder X-ray diffraction pattern for $AgSb_{1-x}Zn_xTe_2$ ($x = 0-0.06$) samples, (b) variation of lattice parameter as a function of Zn (x) concentration in $AgSb_{1-x}Zn_xTe_2$ ($x = 0-0.06$), and (c) DSC curves for $AgSb_{1-x}Zn_xTe_2$ ($x = 0.0, 0.02, 0.04$) samples.

despite their different synthesis procedure such as melting and slow cooling,[29,30] mechanical alloying,[35] and zone melting,[36] which indicates that the matrix is always Sb-rich (Ag-poor) in $AgSbTe_2$. The Ag_2Te impurity may have a negative impact on the thermoelectric properties of $AgSbTe_2$ because of its n-type conduction and structural phase transition at ~425 K.[32] Thus, blocking the formation of the Ag_2Te impurity during synthesis of $AgSbTe_2$ is important for optimization of the thermoelectric and mechanical properties of $AgSbTe_2$. Another major drawback of the $AgSbTe_2$ compound is its low electrical conductivity caused by the heavy hole carriers, which are due to the effect of the flat valence band maximum. Nevertheless, enhancement in the electrical conductivity has been achieved in Na-doped nonstoichiometric $AgSbTe_2$, which exhibited a zT of 1.5 at 570 K.[24]

Cubic $AgSbSe_2$, an analogue of $AgSbTe_2$, is thermodynamically stable below its melting point and shows promising thermoelectric properties for practical application.[37−39] Recently, Du et al. have shown that partial substitution of Se in place of in $AgSbTe_2$ suppresses the formation of impurity phases such as Ag_2Te and $Ag_{0.35}Sb_{0.09}Te_{0.56}$.[32] A zT value of ~1.35 at 565 K is reported for the nominal composition of $AgSbTe_{1.98}Se_{0.02}$.[32] Recently, In doping in $AgSbTe_2$ resulted in a zT of 1.35 at 650 K.[40] Moreover, we have previously shown that Zn doping in $AgSbSe_2$ boosts the thermoelectric

performance through synergistic effect of nanostructuring, carrier engineering, and bond anharmonicity.[38] Motivated by the above fact, we have studied the effect of Zn doping ($x = 0-6$ mol %) on thermoelectric properties of $AgSbTe_2$.

Here, we report a remarkably high thermoelectric figure of merit, zT, of 1.9 at 585 K in p-type $AgSb_{1-x}Zn_xTe_2$ ($x = 0-0.06$) ingots via simultaneous carrier engineering and reduction of lattice thermal conductivity. The zT of 1.9 at 585 K in $AgSb_{0.96}Zn_{0.04}Te_2$ is the highest zT value measured for p-type materials to date in the lower-medium temperature range (450−650 K). Importantly, $AgSb_{0.96}Zn_{0.04}Te_2$ possesses an average thermoelectric figure of merit, zT_{avg}, value of ~1.3 in the 300−600 K range, which is highest value measured to date for $AgSbTe_2$-based compounds. Because Zn^{2+} doping in place of Sb^{3+} in $AgSbTe_2$ acts as an acceptor, it increases p-type carrier concentration and thereby enhances the electrical conductivity. Increased p-type carriers in $AgSb_{1-x}Zn_xTe_2$ easily access the multiple flat valence band valleys in $AgSbTe_2$, which results in a large Seebeck coefficient. In addition, reduction in lattice thermal conductivity was observed upon Zn doping in $AgSbTe_2$ because of phonon scattering due to solid solution point defects. Interestingly, substitution of Zn at a Sb site in $AgSbTe_2$ suppresses the unavoidable formation of Ag_2Te by increasing the solubility of Ag_2Te in $AgSbTe_2$, which indeed increases the thermal and mechanical stability of $AgSbTe_2$. The

maximum hardness value of ~6.3 GPa was measured by nanoindentation method for the $AgSb_{0.96}Zn_{0.04}Te_2$ sample, which is significantly higher than that of the pristine $AgSbTe_2$.

We have synthesized high-quality crystalline ingots of several $AgSb_{1-x}Zn_xTe_2$ (x = 0, 0.02, 0.04, 0.06) compositions by mixing appropriate ratios of high-purity starting materials of Ag, Sb, Zn, and Te in a quartz tube. Quartz tubes were then sealed under vacuum (10^{-5} Torr), slowly heated to 1123 K, then slowly cooled to room temperature (see Experimental Section in the Supporting Information). Bar- and coin-shaped samples obtained after cutting and polishing as-synthesized ingot were used for electrical and thermal transport property measurement, respectively.

Powder X-ray diffraction (PXRD) pattern of $AgSb_{1-x}Zn_xTe_2$ (x = 0, 0.02, 0.04, 0.06) samples could be indexed based on cubic $AgSbTe_2$ structure (space group, $Fm\overline{3}m$) (Figure 1a). Careful analysis of PXRD data for the compositions of x = 0 and x = 0.02 shows the weak diffraction peaks of Ag_2Te, which is consistent with the previously reported literature (Figure S1).[15,17,19] Interestingly, with the addition of Zn (x = 0−6 mol %) in $AgSbTe_2$, impurity peaks corresponding to Ag_2Te become weaker and finally disappear with higher concentration of Zn (Figure S1). This suggests that substitution of Sb with Zn in $AgSbTe_2$ suppresses the formation of the Ag_2Te phase. The lattice parameter of $AgSb_{1-x}Zn_xTe_2$ depends linearly on the concentration of Zn which is consistent with solid solution Vegard's law (Figure 1b).

The DSC curves for $AgSb_{1-x}Zn_xTe_2$ (x = 0, 0.02, 0.04) samples are presented in Figure 1c. A small endothermic peak observed around 425 K is associated with $\alpha-\beta$ structural transition of Ag_2Te for the pristine $AgSbTe_2$ and $AgSb_{0.98}Zn_{0.02}Te_2$. Transition due to Ag_2Te disappears completely for the composition of $x \geq 0.04$, which also confirms the blocking of Ag_2Te formation on Zn doping in $AgSbTe_2$. The exothermic peak around 510 K in the DSC curve is responsible for the appearance of unstable phase Sb_7Te, which is earlier observed in Cu- and Mn-doped $AgSbTe_2$ samples.[41,42] Additionally, one endothermic peak around 602 K is observed for all the samples that correspond to the presence of Ag_5Te_3.[33] The DSC curves show the presence of the large endothermic peak at about 635 K, which corresponds to the decomposition of $AgSbTe_2$ into Ag_2Te and Sb_2Te_3.[33,34] This decomposition limits the thermoelectric studies of $AgSbTe_2$ in the 300−600 K range, and here we have focused our thermoelectric measurement in the same temperature range.

To understand the surface morphology and microstructure compositions, backscattered electron imaging (BSE) and EDS are performed during FESEM measurement. Figure 2 shows BSE-FESEM micrographs of $AgSbTe_2$ (a and b) and $AgSb_{0.96}Zn_{0.04}Te_2$ (c and d) samples. For the pristine $AgSbTe_2$ sample, we have observed nanoprecipitates with lighter contrast with respect to dark contrast $AgSbTe_2$ matrix. EDS analysis indicates that the matrix is Sb-rich $AgSbTe_2$ (Figure S2). The light contrast nanoprecipitates observed in BSE-FESEM are α-Ag_2Te. Substitution of Zn in $AgSbTe_2$ suppresses the formation of Ag_2Te in the matrix; thus, we do not see any nanoprecipitates in $AgSb_{0.96}Zn_{0.04}Te_2$ (Figure 2c,d). We have prepared ingots by a melt−cooling synthesis route. In the cooling process, Ag_2Te with a higher melting point solidifies and slowly grows into microscale precipitates in the $AgSbTe_2$ matrix, resulting in an inhomogeneous multiphase material. With addition of Zn, concentration of Ag_2Te decreases, which
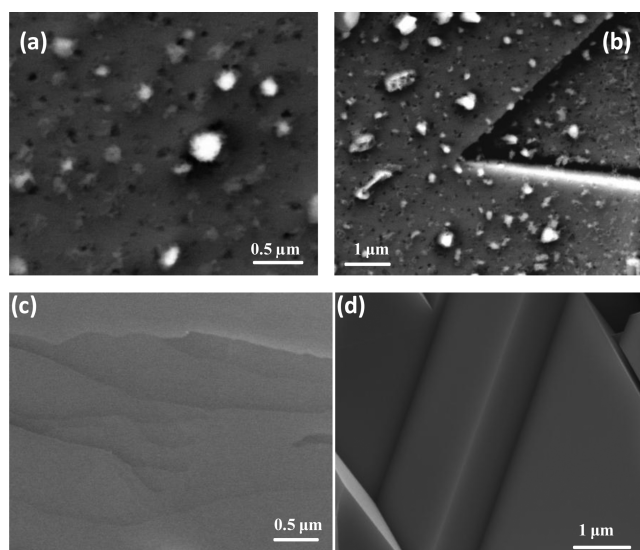
Figure 2. Backscattered electron images taken during FESEM for (a, b) pristine $AgSbTe_2$ and (c, d) $AgSb_{0.96}Zb_{0.04}Te_2$ samples.

is similar to the Se-doped $AgSbTe_2$ sample in which Se helps to reduce the Ag_2Te phase.[32] Actually, Zn increases the solubility limit of Ag_2Te in the $AgSbTe_2$ matrix because Ag_2Te forms a solid solution with ZnTe in the lower concentration range. Similar behavior is observed in GeTe, where 3 mol % Bi_2Te_3 increases the solubility limit of Pb in GeTe.[43]

Figure 3a represents the temperature dependence of electrical conductivity (σ) for $AgSb_{1-x}Zn_xTe_2$ (x = 0−0.06) samples in the 300−635 K range. Aliovalent substitution of Zn^{2+} at Sb^{3+} site in $AgSbTe_2$ increases the σ from ~136 S/cm for pristine $AgSbTe_2$ to ~160 S/cm for $AgSb_{0.96}Zn_{0.04}Te_2$ at 300 K. With the increase in temperature, electrical conductivity of $AgSb_{1-x}Zn_xTe_2$ passes through minima and then starts to increase at high temperature, which is due to the onset of bipolar conduction in a narrow band gap semiconductor. Typically, the $AgSb_{0.96}Zn_{0.04}Te_2$ sample exhibits a σ value of ~160 S/cm at room temperature, which decreases to ~145 S/cm at 475 K and finally increases to ~227 S/cm at 632 K. We observe a small hysteresis in electrical conductivity during the heating−cooling cycle measurement (Figure S6). With addition of Zn (4−6 mol %) in $AgSbTe_2$, the concentration of Ag_2Te decreases significantly, but small amounts of Sb_7Te and Ag_5Te_3 phases still exist in $AgSbTe_2$, which can be shown from the DSC plot of $AgSb_{1-x}Zn_xTe_2$ (Figure 1c). Hysteresis in the temperature dependence of electrical conductivity during heating and cooling cycles occurs because of the unstable phases Sb_7Te and Ag_5Te_3.

To understand the effect of Zn doping on electrical transport behavior in $AgSbTe_2$ system, Hall measurement was carried out to estimate the carrier concentration (n) and carrier mobility (μ) of $AgSb_{1-x}Zn_xTe_2$ samples, which are summarized in Table 1. Doping of Zn in $AgSbTe_2$ increases the p-type carrier concentration from ~1.14×10^{19} cm^{-3} for pristine $AgSbTe_2$ to ~4.8×10^{19} cm^{-3} for the $AgSb_{0.96}Zn_{0.04}Te_2$ sample. This indicates that Zn^{2+} dopes at Sb^{3+} sublattice and contributes one hole per doping in $AgSbTe_2$. Increase in p-type carrier concentration indeed increases the σ in $AgSb_{1-x}Zn_xTe_2$.

Temperature dependence of Seebeck coefficients (S) of $AgSb_{1-x}Zn_xTe_2$ samples are presented in Figure 3b. Positive Seebeck coefficient values indicate p-type conduction, which is consistent with the Hall coefficient data. The Seebeck value for
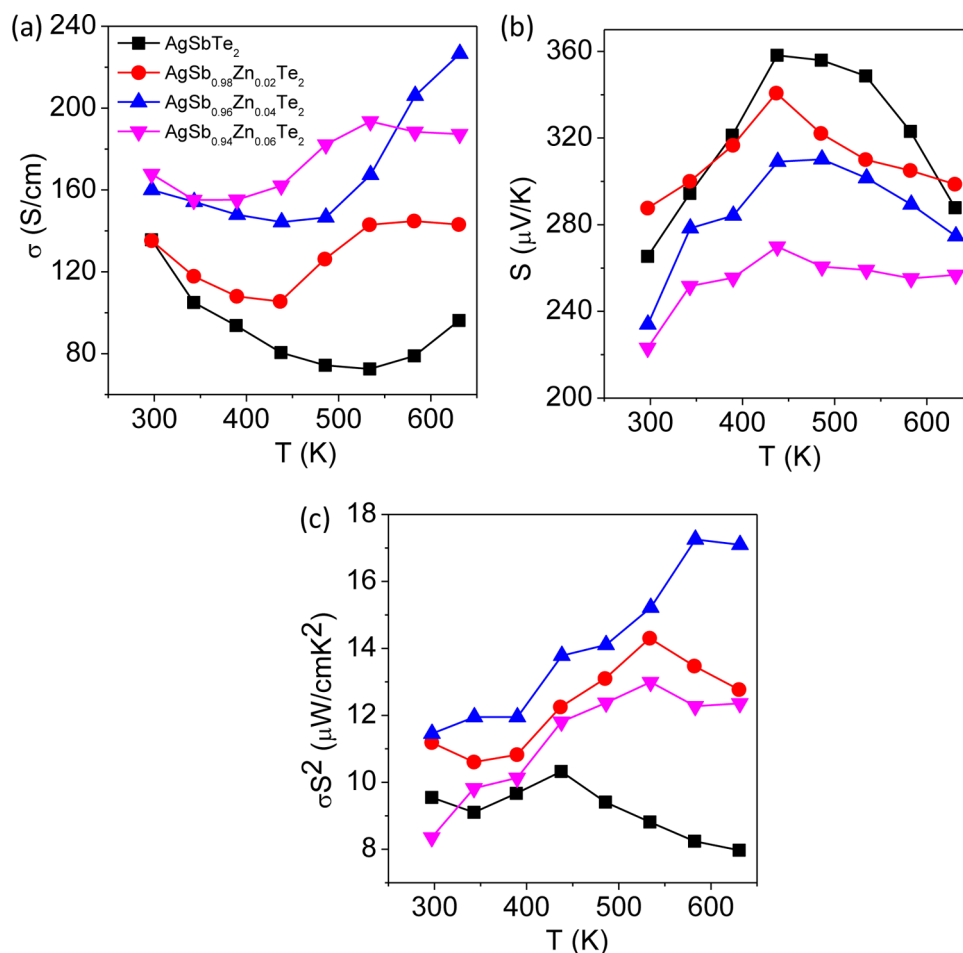
Figure 3. Temperature-dependent (a) electrical conductivity (σ), (b) Seebeck coefficient (S), and (c) power factor (σS^2) for AgSb$_{1-x}$Zn$_x$Te$_2$ (x = 0−0.06) samples.

Table 1. Carrier Concentration (n), Carrier Mobility (μ), and Effective Mass (m^*) of AgSb$_{1-x}$Zn$_x$Te$_2$ (x = 0.0, 0.02, 0.04, and 0.06) Samples at Room Temperature

sample	n (cm^{-3})	μ (cm^2 V^{-1} S^{-1})	m^*
AgSbTe$_2$	1.14×10^{19}	74	$1.32m_0$
AgSb$_{0.98}$Zn$_{0.02}$Te$_2$	2.7×10^{19}	31	$2.82m_0$
AgSb$_{0.96}$Zn$_{0.04}$Te$_2$	4.8×10^{19}	32.5	$2.65m_0$
AgSb$_{0.94}$Zn$_{0.06}$Te$_2$	5.14×10^{19}	20.4	$2.53m_0$

$$S = \pm \frac{k_B}{e} \left(\frac{(r + 3/2)F_{r+3/2}(\eta)}{(r + 3/2)F_{r+1/2}(\eta)} - \eta \right)$$

$$F_n(\eta) = \int_0^\infty \frac{x^n}{1 + e^{x-\eta}} dx$$

where η is the reduced Fermi energy, $F_n(\eta)$ the nth order Fermi integral, k_B the Boltzmann constant, e the electron charge, h the Planck constant, and r the scattering factor. The reduced Fermi energy was extracted based on fitting the respective Seebeck data. Calculated values of m^* for AgSbTe$_2$ and AgSb$_{0.96}$Zn$_{0.04}$Te$_2$ samples are $1.32m_0$ and $2.65m_0$, respectively (Table 1). Similar high m^* values have also been observed in cases of doped AgSbSe$_2$ and AgSbTe$_2$.[37,45,46] The increase in m^* value with the increase in Zn concentration in AgSbTe$_2$ is attributed to increases in p-type carriers, which easily accesses the multiple flat valence band valleys of AgSbTe$_2$. Notably, we have also observed that Zn-doped samples exhibit hole mobility (μ) that is relatively lower than that of the pristine sample because of the presence of heavy holes (Table 1).

Figure 3c represents the temperature-dependent power factors (σS^2) for AgSb$_{1-x}$Zn$_x$Te$_2$ samples. Typically, AgSbTe$_2$ exhibits the $S^2\sigma$ value of ~9.6 μW cm^{-1} K^{-2} at 300 K, which decreases to ~7.9 μW cm^{-1} K^{-2} at 610 K. However, the AgSb$_{0.96}$Zn$_{0.04}$Te$_2$ sample exhibits the $S^2\sigma$ value of ~11.5 μW cm^{-1} K^{-2} at 300 K, which reaches the maximum value of ~17.3 μW cm^{-1} K^{-2} at 585 K.

the pristine AgSbTe$_2$ sample is ~264 μV/K at room temperature, which increases to ~360 μV/K at ~438 K. The large Seebeck value of AgSbTe$_2$ is attributed to the presence of a flat and multivalley valence band.[26] Typically, the AgSb$_{0.96}$Zn$_{0.04}$Te$_2$ sample shows a room-temperature Seebeck value of ~235 μV/K which increases to ~275 μV/K at 610 K. The high S value in AgSbTe$_2$-based compounds is due to high density of state effective mass (m^*). Assuming a single parabolic band model with acoustic phonon scattering (r = −1/2), we have estimated the m^* according to the following equation using the measured Seebeck coefficients and Hall carrier concentrations (n):[37,44,45]

$$m^* = \frac{h^2}{2Tk_B} \left[\frac{n}{4\pi F_{1/2}(\eta)} \right]^{2/3}$$

Figure 4. Temperature-dependent (a) total thermal conductivity (κ_{total}) and (b) lattice thermal conductivity (κ_{latt}) for AgSb$_{1-x}$Zn$_x$Te$_2$ ($x = 0-$0.06) samples.
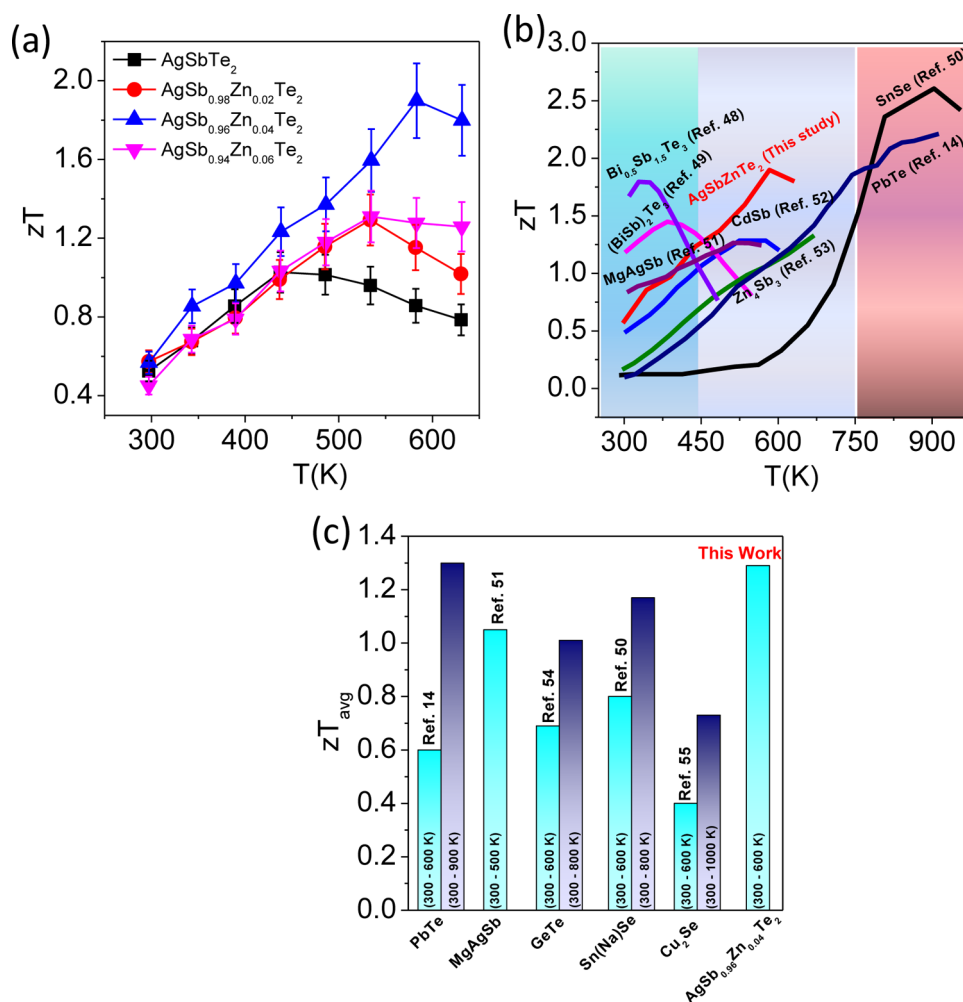
Figure 5. (a) Temperature-dependent thermoelectric figure of merit (zT) of AgSb$_{1-x}$Zn$_x$Te$_2$ ($x = 0-0.06$) samples. (b) The best zT obtained in this study compared with some of the state-of-the-art thermoelectric materials. The p-type Zn-doped AgSbTe$_2$ shows the highest zT in the lower-medium temperature range (450−650 K). (c) zT$_{avg}$ values for several popular polycrystalline thermoelectric materials compared with the present AgSb$_{1-x}$Zn$_x$Te$_2$.

Temperature-dependent thermal conductivities of AgSb$_{1-x}$Zn$_x$Te$_2$ samples are illustrated in Figure 4. The total thermal conductivities, κ_{total}, of all the samples were estimated by using the formula $\kappa_{total} = DC_p\rho$, where D is the thermal diffusivity (Figure S3a), C_p the specific heat (Figure S4), and ρ the density (Table S2) of the sample in the temperature range of 300−650 K. At 300 K, κ_{total} values for all the samples range from 0.55 W/mK to 0.65 W/mK, which agree with previous

results.[17,21−24] However, with increasing temperature, we observe the enhanced contribution of bipolar thermal conductivity, which is typical of a narrow band gap semiconductor. Previous theoretical electronic structure calculation indicates that AgSbTe$_2$ exhibits a semimetallic band structure where the conduction band goes below the top of the valence band.[26] It is well-known that most density functional theory calculations tend to underestimate the band gaps of semiconductors, and we cannot exclude the possibility that AgSbTe$_2$ is a semiconductor with a small band gap. Previous diffuse reflectance measurement in AgSbTe$_2$ provided an apparent band gap (0.35 eV), whereas electrical conductivity suggested a band gap of 0.1 eV.[26] These results clearly indicate that AgSbTe$_2$ is a narrow band gap semiconductor. Substitution of a small amount of Zn at the position of Sb in AgSbTe$_2$ does not change the narrow band gap nature of AgSbTe$_2$, which can be seen from temperature-dependent thermal conductivity which shows similar onset temperature for bipolar thermal conduction compared to pristine AgSbTe$_2$.

κ_{total} of AgSb$_{1−x}$Zn$_x$Te$_2$ is mainly governed by its lattice component, κ_{latt}, which corresponds to proliferation of phonons. Temperature-dependent κ_{latt} for AgSb$_{1−x}$Zn$_x$Te$_2$ samples were estimated by subtracting electronic thermal conductivity ($\kappa_{el} = L\sigma T$ (Figure S3b)), where L is the Lorenz number which can be obtained based on the fitting of the respective Seebeck values that estimate the reduced chemical potential as explained elsewhere[37]) from κ_{total}. The intrinsically low thermal conductivity of AgSbTe$_2$ arises because of the presence of strong bond anharmonicity, resulting from the stereochemically active 5s^2 lone pair on Sb, which deforms lattice vibration significantly.[17] At 600 K, the AgSb$_{0.96}$Zn$_{0.04}$Te$_2$ sample exhibits a κ_{latt} value of ∼0.36 W/mK, which reaches close to the theoretical minimum limit of the thermal conductivity (∼0.3 W/mK) in AgSbTe$_2$ calculated using the formula described by Cahill et al.[47] Reduction in the lattice thermal conductivity was ∼26% in AgSb$_{0.96}$Zn$_{0.04}$Te$_2$ when compared to the pristine AgSbTe$_2$. The decrease in κ_{latt} of AgSb$_{0.96}$Zn$_{0.04}$Te$_2$ compared to that of pristine AgSbTe$_2$ is due to scattering of heat-carrying phonons via solid solution point defects.

We have estimated the dimensionless figure of merit (zT) for AgSb$_{1−x}$Zn$_x$Te$_2$ (x = 0, 0.02, 0.04, 0.06) samples by using measured values of σ, S, and κ in the 300−635 K temperature range (Figure 5a). Although, room-temperature zT values of all the samples were comparable, the advantage of addition of Zn is clearly distinguishable at elevated temperatures. We have obtained a maximum zT of ∼1.9 at ∼585 K for AgSb$_{0.96}$Zn$_{0.04}$Te$_2$, which is significantly higher compared to that of the pristine AgSbTe$_2$ sample and other reported values for doped AgSbTe$_2$ (Figure S5).

The p-type Bi$_{0.5}$Sb$_{1.5}$Te$_3$[48,49] based materials exhibit high performance in the 300−400 K range, whereas p-type PbTe[14] and SnSe[50] based materials show high performance in the 700−900 K range (Figure 5b). High-performance p-type materials are desirable in the 450−650 K range for lower-medium temperature power generation applications. p-type MgAgSb,[51] CdSb,[52] and Zn$_4$Sb$_3$[53] based materials show promising performance in the 450−650 K range (Figure 5b). p-type AgSb$_{0.96}$Zn$_{0.04}$Te$_2$ exhibits zT of 1.9 at 584 K, which is the highest value obtained in the 450−650 K range among the p-type materials. The average zT value (zT$_{avg}$) of AgSb$_{0.96}$Zn$_{0.04}$Te$_2$ is estimated to be ∼1.3 by considering the cold and hot side temperatures of 300 and 600 K, respectively,

which is on par with that of high-performance state-of-the-art thermoelectric materials (Figure 5c).[14,50,51,54,55]

In addition to high zT and high zT$_{avg}$, materials should possess high mechanical stability for device applications. The mechanical properties, reduced elastic modules and hardness, of AgSb$_{1−x}$Zn$_x$Te$_2$ samples were measured by the nanoindentation method (Table S1). Figure 6 shows the load (P) versus
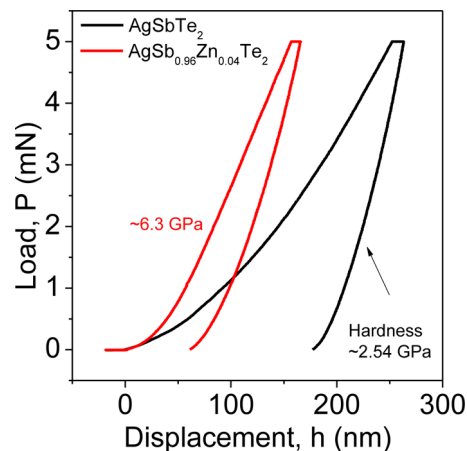
Figure 6. Load (P) vs displacement (h) curve and hardness value (GPa) of AgSb$_{1−x}$Zn$_x$Te$_2$ (x = 0.0, 0.04) samples measured by nanoindentation.

displacement (h) curves of AgSbTe$_2$ and AgSb$_{0.96}$Zn$_{0.04}$Te$_2$ samples. The pristine AgSbTe$_2$ sample possesses the hardness value of ∼2.54 GPa, whereas the AgSb$_{0.96}$Zn$_{0.04}$Te$_2$ sample shows the maximum hardness value of ∼6.3 GPa. Substitution of Zn in AgSbTe$_2$ increases the hardness of the matrix significantly by increasing the rigidity of the material. Generally, hardness or strength of materials can be defined by dislocation motion in the lattice of the matrix material.[56] Hardness can be effectively controlled by introducing solid solution, grain boundaries, and second phase nanoprecipitates in the matrix, where solute atoms in solid solution, grain boundaries, and small nanoprecipitates impede the motion of a dislocation, thereby increasing the strength and hardness of the material.[57] Because Zn doping increases the solubility of Ag$_2$Te in the AgSbTe$_2$ matrix, we anticipate that the increased point defects due to solid solution impede the dislocation propagation, thereby enhancing the hardness of the material. This result indicates that Zn-doped AgSbTe$_2$-based materials have a significantly high mechanical stability, which is useful during large-scale device fabrication.

In summary, crystalline ingots of p-type AgSb$_{1−x}$Zn$_x$Te$_2$ exhibit a zT of 1.9 at 585 K, which is the highest in the lower-medium temperature range (450−600). An average zT$_{avg}$ value of 1.3 is obtained in the 300−600 K range for the AgSb$_{0.96}$Zn$_{0.04}$Te$_2$ sample, which is comparable to that of the best polycrystalline thermoelectric materials. Moreover, we have achieved a hardness value of ∼6.3 GPa for the high-performance AgSb$_{0.96}$Zn$_{0.04}$Te$_2$ sample, which is significantly higher than that of the pristine AgSbTe$_2$. Zn doping in AgSbTe$_2$ suppresses the formation of the Ag$_2$Te impurity phase, which indeed increases the thermal and mechanical stability. Zn^{2+} acts as an acceptor dopant in AgSbTe$_2$, thereby enhancing the electrical conductivity and power factor. Moreover, the lattice thermal conductivities for AgSb$_{1−x}$Zn$_x$Te$_2$

samples were reduced substantially because of the increased phonon scattering resulting from solid solution point defects.

■ ASSOCIATED CONTENT

ⓢ Supporting Information

The Supporting Information is available free of charge on the ACS Publications website at DOI: 10.1021/acsenergy-lett.6b00639.

> Experimental section; zoomed PXRD (Figure S1); EDS for $AgSbTe_2$ (Figure S2); diffusivity and electrical thermal conductivity for $AgSb_{1-x}Zn_xTe_2$ (Figure S3); deatiled specific heat for $AgSbTe_2$ (Figure S4); comparison of zT_{max} and zT_{avg} of $AgSbTe_2$-based materials (Figure S5); heating and cooling cycle for $AgSb_{1-x}Zn_xTe_2$ samples (Figures S6 and S7); reproducibility of thermoelectric figure of merit (zT) for a typical sample (Figure S8); electrical transport data of two bars from different parts of the same ingot of $AgSbTe_2$ (Figure S9); reduced elastic modules and hardness values (Table S1) and densities of $AgSb_{1-x}Zn_xTe_2$ samples (Table S2); EDAX of two bars from different parts of the same ingot of $AgSbTe_2$ (Table S3) (PDF)

■ AUTHOR INFORMATION

Corresponding Author

*E-mail: kanishka@jncasr.ac.in.

ORCID Ⓞ

Kanishka Biswas: 0000-0001-9119-2455

Notes

The authors declare no competing financial interest.

■ ACKNOWLEDGMENTS

■ REFERENCES

(1) Sootsman, J.; Chung, D. Y.; Kanatzidis, M. G. New and old concepts in thermoelectric materials. *Angew. Chem., Int. Ed.* 2009, 48, 8616−8639.

(2) Tan, G.; Zhao, L. D.; Kanatzidis, M. G. Rationally designing high-performance bulk thermoelectric materials. *Chem. Rev.* 2016, 116, 12123−12149.

(3) Zhao, L. D.; Dravid, V. P.; Kanatzidis, M. G. The panoscopic approach to high performance thermoelectrics. *Energy Environ. Sci.* 2014, 7, 251−268.

(4) Kim, H. S.; Liu, W.; Chen, G.; Chu, C.-W.; Ren, Z. Relationship between thermoelectric figure of merit and energy conversion efficiency. *Proc. Natl. Acad. Sci. U. S. A.* 2015, 112, 8205−8210.

(5) Perumal, S.; Roychowdhury, S.; Biswas, K. High performances thermoelectric materials and devices based on GeTe. *J. Mater. Chem. C* 2016, 4, 7520−7536.

(6) Heremans, J. P.; Jovovic, V.; Toberer, E. S.; Saramat, A.; Kurosaki, K.; Charoenphakdee, A.; Yamanaka, S.; Snyder, G. J. Enhancement of thermoelectric efficiency in PbTe by distortion of the electronic density of states. *Science* 2008, 321, 554−557.

(7) Zhang, Q.; Liao, B.; Lan, Y.; Lukas, K.; Liu, W.; Esfarjani, K.; Opeil, C.; Broido, D.; Chen, G.; Ren, Z. High thermoelectric performance by resonant dopant indium in nanostructured SnTe. *Proc. Natl. Acad. Sci. U. S. A.* 2013, 110, 13261−13266.

(8) Pei, Y.; Shi, X.; LaLonde, A.; Wang, H.; Chen, L.; Snyder, G. J. Convergence of electronic bands for high performance bulk thermoelectrics. *Nature* 2011, 473, 66−69.

(9) Banik, A.; Shenoy, U. S.; Saha, S.; Waghmare, U. V.; Biswas, K. High power factor and enhanced thermoelectric performance of SnTe-AgInTe$_2$: synergistic effect of resonance level and valence band convergence. *J. Am. Chem. Soc.* 2016, 138, 13068−13075.

(10) Roychowdhury, S.; Shenoy, U. S.; Waghmare, U. V.; Biswas, K. Tailoring of electronic structure and thermoelectric properties of a topological crystalline insulator by chemical doping. *Angew. Chem., Int. Ed.* 2015, 54, 15241−15245.

(11) Biswas, K.; He, J.; Zhang, Q.; Wang, G.; Uher, C.; Dravid, V. P.; Kanatzidis, M. G. Strained endotaxial nanostructures with high thermoelectric figure of merit. *Nat. Chem.* 2011, 3, 160−166.

(12) Zhao, L. D.; Hao, S.; Lo, S. H.; Wu, C. I.; Zhou, X.; Lee, Y.; Li, H.; Biswas, K.; Hogan, T. P.; Uher, C.; et al. High thermoelectric performance via hierarchical compositionally alloyed nanostructures. *J. Am. Chem. Soc.* 2013, 135, 7364−7370.

(13) Banik, A.; Vishal, B.; Perumal, S.; Datta, R.; Biswas, K. The origin of low thermal conductivity in Sn$_{1-x}$Sb$_x$Te: phonon scattering via layered intergrowth nanostructures. *Energy Environ. Sci.* 2016, 9, 2011−2019.

(14) Biswas, K.; He, J.; Blum, I. D.; Wu, C. I.; Hogan, T. P.; Seidman, D. N.; Dravid, V. P.; Kanatzidis, M. G. High-performance bulk thermoelectrics with all-scale hierarchical architectures. *Nature* 2012, 489, 414−418.

(15) Poudel, B.; Hao, Q.; Ma, Y.; Lan, Y.; Minnich, A.; Yu, B.; Yan, X.; Wang, D.; Muto, A.; Vashaee, D.; et al. High-thermoelectric performance of nanostructured bismuth antimony telluride bulk alloys. *Science* 2008, 320, 634−638.

(16) Zhao, L. D.; Lo, S. H.; Zhang, Y.; Sun, H.; Tan, G.; Uher, C.; Wolverton, C.; Dravid, V. P.; Kanatzidis, M. G. Ultralow thermal conductivity and high thermoelectric figure of merit in SnSe crystals. *Nature* 2014, 508, 373−377.

(17) Morelli, D. T.; Jovovic, V.; Heremans, J. P. Intrinsically minimal thermal conductivity in cubic I-V-VI$_2$ semiconductors. *Phys. Rev. Lett.* 2008, 101, 035901.

(18) Guin, S. N.; Pan, J.; Bhowmik, A.; Sanyal, D.; Waghmare, U. V.; Biswas, K. Temperature dependent reversible p−n−p type conduction switching with colossal change in thermopower of semiconducting AgCuS. *J. Am. Chem. Soc.* 2014, 136, 12712−12720.

(19) Shi, X.; Yang, J.; Salvador, J. R.; Chi, M.; Cho, J. Y.; Wang, H.; Bai, S.; Yang, J.; Zhang, W.; Chen, L. Multiple-filled skutterudites: high thermoelectric figure of merit through separately optimizing electrical and thermal transports. *J. Am. Chem. Soc.* 2011, 133, 7837−7846.

(20) Jana, M. K.; Pal, K.; Waghmare, U. V.; Biswas, K. The Origin of Ultralow thermal conductivity in InTe: lone-pair-induced anharmonic rattling. *Angew. Chem., Int. Ed.* 2016, 55, 7792−7796.

(21) Ma, J.; Delaire, O.; May, A. F.; Carlton, C. E.; McGuire, M. A.; VanBebber, L. H.; Abernathy, D. L.; Ehlers, G.; Hong, T.; Huq, A.; et al. Glass-like phonon scattering from a spontaneous nanostructure in AgSbTe$_2$. *Nat. Nanotechnol.* 2013, 8, 445−451.

(22) Zhang, S. N.; Zhu, T. J.; Yang, S. H.; Yu, C.; Zhao, X. B. Phase compositions, nanoscale microstructures and thermoelectric properties in Ag$_{2-y}$Sb$_y$Te$_{1+y}$ alloys with precipitated Sb$_2$Te$_3$ plates. *Acta Mater.* 2010, 58, 4160−4169.

(23) Nielsen, M. D.; Ozolins, V.; Heremans, J.-P. Lone pair electrons minimize lattice thermal conductivity. *Energy Environ. Sci.* 2013, 6, 570−578.

(24) Du, B. L.; Li, H.; Tang, X. F. Enhanced thermoelectric performance in Na-doped p-type non-stoichiometric AgSbTe$_2$ compound. *J. Alloys Compd.* 2011, 509, 2039−2043.

(25) Armstrong, R. W.; Faust, J. W.; Tiller, W. A. A structural study of the compound AgSbTe$_2$. *J. Appl. Phys.* 1960, 31, 1954.

(26) Hoang, K.; Mahanti, S. D.; Salvador, J. R.; Kanatzidis, M. G. Atomic ordering and gap formation in Ag-Sb-based ternary chalcogenides. *Phys. Rev. Lett.* 2007, 99, 156403.

(27) Hsu, K. F.; Loo, S.; Guo, F.; Chen, W.; Dyck, J. S.; Uher, C.; Hogan, T.; Polychroniadis, E. K.; Kanatzidis, M. G. Cubic AgPb$_m$SbTe$_{2+m}$: bulk thermoelectric materials with high figure of merit. *Science* 2004, 303, 818−821.

(28) Rosi, F. D.; Dismukes, J. P.; Hockings, E. F. Semiconductor materials for thermoelectric power generation up to 700 C. *Electr. Eng.* **1960**, *79*, 450.

(29) Wojciechowski, K. T.; Schmidt, M. Structural and thermoelectric properties of AgSbTe$_2$-AgSbSe$_2$ pseudo-binary system. *Phys. Rev. B: Condens. Matter Mater. Phys.* **2009**, *79*, 184202.

(30) Sugar, J. D.; Medlin, D. L. Precipitation of Ag$_2$Te in the thermoelectric material AgSbTe$_2$. *J. Alloys Compd.* **2009**, *478*, 75–82.

(31) Ayralmarin, R. M.; Brun, G.; Maurin, M.; Tedenac, J. C. Contribution to the study of AgSbTe$_2$. *Eur. J. Solid State Inorg. Chem.* **1990**, *27*, 747–757.

(32) Du, B.; Li, H.; Xu, J.; Tang, X.; Uher, C. Enhanced figure-of-merit in Se-doped p-type AgSbTe$_2$ thermoelectric compound. *Chem. Mater.* **2010**, *22*, 5521–5527.

(33) Wyzga, P. M.; Wojciechowski, K. T. Analysis of the influence of thermal treatment on the stability of Ag$_{1-x}$Sb$_{1+x}$Te$_{2+x}$ and Se-doped AgSbTe$_2$. *J. Electron. Mater.* **2016**, *45*, 1548–1554.

(34) Du, B.; Yan, Y.; Tang, X. Variable-temperature in situ X-ray diffraction study of the thermodynamic evolution of AgSbTe$_2$ thermoelectric compound. *J. Electron. Mater.* **2015**, *44*, 2118–2123.

(35) Wang, H.; Li, J.; Zou, M.; Sui, T. Synthesis and transport property of AgSbTe$_2$ as a promising thermoelectric compound. *Appl. Phys. Lett.* **2008**, *93*, 202106.

(36) Wolfe, R.; Wernick, J.; Haszko, S. Anomalous hall effect in AgSbTe$_2$. *J. Appl. Phys.* **1960**, *31*, 1959–1964.

(37) Guin, S. N.; Chatterjee, A.; Negi, D. S.; Datta, R.; Biswas, K. High thermoelectric performance in tellurium free p-type AgSbSe$_2$. *Energy Environ. Sci.* **2013**, *6*, 2603–2608.

(38) Guin, S. N.; Negi, D. S.; Datta, R.; Biswas, K. Nanostructuring, carrier engineering and bond anharmonicity synergistically boost the thermoelectric performance of p-type AgSbSe$_2$–ZnSe. *J. Mater. Chem. A* **2014**, *2*, 4324–4331.

(39) Guin, S. N.; Biswas, K. Sb deficiencies control hole transport and boost the thermoelectric performance of p-type AgSbSe$_2$. *J. Mater. Chem. C* **2015**, *3*, 10415–10421.

(40) Mohanraman, R.; Sankar, R.; Boopathi, K. M.; Chou, F.-C.; Chu, C.-W.; Lee, C.-H.; Chen, Y.-Y. Influence of In doping on the thermoelectric properties of an AgSbTe$_2$ compound with enhanced figure of merit. *J. Mater. Chem. A* **2014**, *2*, 2839–2844.

(41) Zhang, H.; Luo, J.; Zhu, H. T.; Liu, Q. L.; Liang, J. K.; Rao, G. H. Phase stability, crystal structure and thermoelectric properties of Cu doped AgSbTe$_2$. *Acta Phys. Sin.* **2012**, *61*, 086101.

(42) Zhang, H.; Luo, J.; Zhu, H.-T.; Liu, Q.-L.; Liang, J.-K.; Li, J.-B.; Liu, G.-Y. Synthesis and thermoelectric properties of Mn-doped AgSbTe$_2$ compounds. *Chin. Phys. B* **2012**, *21*, 106101.

(43) Wu, D.; Zhao, L.-D.; Hao, S.; Jiang, Q.; Zheng, F.; Doak, J. W.; Wu, H.; Chi, H.; Gelbstein, Y.; Uher, C.; et al. Origin of the high performance in GeTe-based thermoelectric materials upon Bi$_2$Te$_3$ doping. *J. Am. Chem. Soc.* **2014**, *136*, 11412–11419.

(44) Wojciechowski, K. T.; Schmidt, M. Structural and thermoelectric properties of AgSbTe$_2$-AgSbSe$_2$ pseudobinary system. *Phys. Rev. B: Condens. Matter Mater. Phys.* **2009**, *79*, 184202.

(45) Jovovic, V.; Heremans, J. P. Measurements of the energy band gap and valence band structure of AgSbTe$_2$. *Phys. Rev. B: Condens. Matter Mater. Phys.* **2008**, *77*, 245204.

(46) Wojciechowski, K.; Tobola, J.; Schmidt, M.; Zybala, R. Crystal structure, electronic and transport properties of AgSbSe$_2$ and AgSbTe$_2$. *J. Phys. Chem. Solids* **2008**, *69*, 2748–2755.

(47) Cahill, D. G.; Watson, S. K.; Pohl, R. O. Lower limit to the thermal conductivity of disordered crystals. *Phys. Rev. B: Condens. Matter Mater. Phys.* **1992**, *46*, 6131–6140.

(48) Kim, S.; Lee, K. H.; Mun, H. A.; Kim, H. S.; Hwang, S. W.; Roh, J. W.; Yang, D. J.; Shin, W. H.; Li, X. S.; Lee, Y. H.; et al. Dense dislocation arrays embedded in grain boundaries for high-performance bulk thermoelectrics. *Science* **2015**, *348*, 109–113.

(49) Poudel, B.; Hao, Q.; Ma, Y.; Lan, Y.; Minnich, A.; Yu, B.; Yan, X.; Wang, D.; Muto, A.; Vashaee, D.; et al. High-thermoelectric performance of nanostructured bismuth antimony telluride bulk alloys. *Science* **2008**, *320*, 634–638.

(50) Peng, K.; Lu, X.; Zhan, H.; Hui, S.; Tang, X.; Wang, G.; Dai, J.; Uher, C.; Wang, G.; Zhou, X. Broad temperature plateau for high ZTs in heavily doped p-type SnSe single crystals. *Energy Environ. Sci.* **2016**, *9*, 454–460.

(51) Shuai, J.; Kim, H. S.; Lan, Y. C.; Chen, S.; Liu, Y.; Zhao, H. Z.; Sui, J. H.; Ren, Z. F. Study on thermoelectric performance by Na doping in nanostructured Mg$_{1-x}$Na$_x$Ag$_{0.97}$Sb$_{0.99}$. *Nano Energy* **2015**, *11*, 640–646.

(52) Wang, S.; Yang, J.; Wu, L.; Wei, P.; Yang, J.; Zhang, W.; Grin, Y. Anisotropic multicenter bonding and high thermoelectric performance in electron-poor CdSb. *Chem. Mater.* **2015**, *27*, 1071–1081.

(53) Snyder, G. J.; Christensen, M.; Nishibori, E.; Caillat, T.; Iversen, B. B. Disordered zinc in Zn$_4$Sb$_3$ with phonon-glass and electron-crystal thermoelectric properties. *Nat. Mater.* **2004**, *3*, 458–463.

(54) Perumal, S.; Roychowdhury, S.; Negi, D. S.; Datta, R.; Biswas, K. High thermoelectric performance and enhanced mechanical stability of Pb-free p-type Ge$_{1-x}$Sb$_x$Te. *Chem. Mater.* **2015**, *27*, 7171–7178.

(55) Liu, H.; Shi, X.; Xu, F.; Zhang, L.; Zhang, W.; Chen, L.; Li, Q.; Uher, C.; Day, T.; Snyder, G. J. Copper ion liquid-like thermoelectrics. *Nat. Mater.* **2012**, *11*, 422–425.

(56) Lu, K.; Lu, L.; Suresh, S. Strengthening materials by engineering coherent internal boundaries at the nanoscale. *Science* **2009**, *324*, 349–352.

(57) Zandbergen, H. W.; Andersen, S. J.; Jansen, J. Structure determination of Mg$_5$Si$_6$ particles in Al by dynamic electron diffraction studies. *Science* **1997**, *277*, 1221–1225.